Uptake of iodide by calcium aluminate phases (AFm phases)

Nedyalkova, L.[1,2),*], Lothenbach, B.[1)], Geng, G.[2)], Mäder, U.[3)], Tits, J.[2)]

[1)] Laboratory for Concrete and Construction Chemistry, Empa, Dübendorf, Switzerland

[2)] Laboratory for Waste Management, Paul Scherrer Institute, Villigen PSI, Switzerland

[3)] Institute of Geological Sciences, University of Bern, Switzerland

*Corresponding author. E-mail address: latina.nedyalkova@empa.ch; latina_nedyalkova@abv.bg

Keywords: AFm phases, iodine, waste management, solid solution, thermodynamic modelling

Abstract

Iodine-129 is an important dose-determining radionuclide emanating from low and intermediate level radioactive waste (L/ILW) repositories. A good candidate for the immobilization of the hazardous I^- anions are AFm phases due to their interlayer anion exchange capacity.

The ability of AFm phases to bind iodine was investigated in a set of co-precipitation experiments, in which the formation of solid solutions between the iodine AFm end member monoiodide (I-AFm) and the common AFm phases hemicarbonate (OH,CO_3-AFm), monocarbonate (CO_3-AFm) and hydroxy-AFm (OH-AFm), was examined. The samples were characterized by TGA, FTIR, XRPD and liquid phase analyses, and the obtained data were used to construct solid solution models with the help of the thermodynamic modelling program GEMS. The formation of extensive solid solutions was found between the AFm end member pairs monoiodide and hydroxy-AFm, and monoiodide and hemicarbonate. In these two cases, the progressive substitution of the interlayer anion is reflected by a gradual change of the interlayer distance, visible by a continuous peak shift of the basal reflexion from one end member towards the other. No solid solution forms between the end members monoiodide and monocarbonate. In the presence of small amounts of carbonate, a mixed (I,OH,CO_3)-AFm phase precipitates, similar to the one found in the monoiodide-hemicarbonate set of experiments, indicated by the similarity in the observed d-values. With increasing carbonate concentration, monocarbonate is stabilized.

The experimental data suggests that iodine can be incorporated in the AFm interlayer where anion exchange leads to the formation of solid solutions. The solid solution formation is favoured only between end members with similar crystal symmetry. The presence of carbonate favours the formation of monocarbonate in the long term, reducing the capability of AFm phases to immobilize iodide.

1. Introduction

Iodine-129 is a long-lived radionuclide (with a half-life of 1.57×10^7 a) present in low and intermediate level radioactive waste (L/ILW) and therefore of importance with a view to the safe disposal of this kind of waste (NAGRA 2002). Under the alkaline ($10 < pH < 13.5$) and reducing conditions (-750 mV $< E_h < -230$ mV (SHE)) expected in the near-field of a cement-based L/ILW repository (Wersin et al. 2003), the thermodynamically stable iodine species is iodide (I^-). The migration of the I^- anions through the repository near-field can be retarded by sorption on the cementitious materials used for the construction of the engineered barrier system. Amongst the components of the cementitious matrix, AFm (Al_2O_3-Fe_2O_3-mono) phases are the minerals with the highest sorption capacity for I^- (Atkins and Glasser 1992). AFm phases are a group of layered calcium aluminate-ferrite double hydroxides (LDH family) with the general formula $[Ca_4(Al,Fe)_2(OH)_{12}]\cdot X\cdot nH_2O$. The structure is built by octahedral calcium-aluminium hydroxide layers with a Ca^{2+}:Al^{3+}(Fe^{3+}) ratio of 2:1 ($[Ca_4(Al,Fe)_2(OH)_{12}]^{2+}$), alternating with interlayers containing charge-balancing X anions and water molecules ($[X\cdot nH_2O]^{2-}$) (Taylor 1997). The type of the X anion and the amount of interlayer water *n* determine the layer thickness (Taylor 1997, Baquerizo et al. 2015). A variety of mono- or divalent anions can serve as X depending on the cement composition and the service environment (e.g. repository near-field), the most common ones being CO_3^{2-}, OH^-, SO_4^{2-} and Cl^- (Evans and Slade 2006, Matschei et al. 2007a). An AFm phase may also contain more than one type of interlayer anions, leading to the formation of solid solutions (Glasser et al. 1999, Matschei et al. 2007a).

The high interlayer anion exchange capacity of AFm phases makes them a suitable candidate for the immobilization of the I^- anions. A number of studies have been carried out investigating the structural incorporation of I^- in the AFm interlayer (Brown and Grutzeck 1985, Rapin et al. 1999, Toyohara et al. 2000, Aimoz et al. 2012a). The existence of a stable monoiodide (I-AFm) phase with the composition $3CaO\cdot Al_2O_3\cdot CaI_2\cdot 10H_2O$ has been confirmed and its structure solved in the trigonal R-3H space group with an interlayer spacing of 8.84 Å (Rapin et al. 1999). The synthesis of bianionic AFm phases containing a mixture of I^- and another type of anion in the interlayer have also been attempted, showing that the incorporation of I^- is dependent on the type of the competing anion. The I-AFm phase was found to form continuous solid solutions with the Br-AFm (Kuzel 1971) and the SO_4-AFm (monosulfate) (Kuzel 1971, Aimoz et al. 2012a, 2012b). The thermodynamic properties of the (I,SO_4)-AFm solid solution were also determined (Aimoz et al. 2012b). On the other hand, the presence of Cl^- favours the precipitation of Cl-AFm (Friedel's salt) in coexistence with an I-AFm rather than forming a solid solution (Kuzel 1971, Aimoz et al. 2012a). In the case of CO_3^{2-} as the competitive anion, Aimoz et al.

(2012a) observed destabilization of the I-AFm and its partial recrystallization into CO_3-AFm (monocarbonate) in a set of experiments, where CO_3^{2-} was added to an I-AFm suspension. In co-precipitation experiments, however, the same authors found the formation of a mixed AFm phase with two distinct types of interlayer regions – one filled by I^- only and another one by OH^- and CO_3^{2-} (corresponding to hemicarbonate, an (OH,CO_3)-AFm); stacked sequentially in an almost regular pattern. The resulting AFm phase had an interlayer distance of 17.01 Å, consistent with the interstratification of I-AFm and (OH,CO_3)-AFm. Such stacking effect has also been reported for Kuzel's salt, an (Cl,SO_4)-AFm, whose structure is composed of the intercalation of the two end members Cl-AFm and SO_4-AFm (Mesbah et al. 2011a).

Modern cements contain in addition to cement clinkers and calcium sulfate, also limestone, which prevents the formation of monosulfate (SO_4-AFm), while initially hemicarbonate (OH,CO_3-AFm), and later monocarbonate (CO_3-AFm) is formed (Lothenbach et al. 2008, Zajac et al. 2014). Thus, the present study concentrates on I^- uptake by AFm phases in competition with CO_3^{2-} and/or OH^- and the possible formation of solid solutions between the different AFm end members. A short summary of the AFm phases occurring in the CaO-Al_2O_3-(CO_2)-H_2O system and their relevant characteristics follows. Monocarbonate (Mc), with the chemical formula $3CaO \cdot Al_2O_3 \cdot CaCO_3 \cdot 11H_2O$, has a triclinic symmetry and two known structures – an ordered one with the P1 space group (Francois et al. 1998) and a disordered structure described in the P-1 space group (Renaudin et al. 1999). The CO_3^{2-} anions from the interlayer are connected to the Ca^{2+} from the main layer via shared oxygens belonging to the carbonate group, thus resulting in a very rigid structure and a narrow interlayer distance of 7.55 Å (Francois et al. 1998). In the hemicarbonate (Hc) structure half of the carbonate in the interlayer is replaced by hydroxyl groups (OH^-) corresponding to the formula $3CaO \cdot Al_2O_3 \cdot 0.5(Ca(OH)_2) \cdot 0.5(CaCO_3) \cdot 11.5H_2O$. The interlayer anions are bonded only weakly to the main layer by hydrogen bonds, giving rise to a different crystal symmetry (trigonal, R-3cH space group) and larger interlayer distance (d = 8.20 Å) (Runčevski et al. 2012). In the presence of carbonate concentrations above the stability limit for hemicarbonate, it is unstable and slowly transforms to monocarbonate (Kuzel and Pöllmann 1991, Lothenbach et al. 2008). As an intermediate product of this transformation another phase can form – the carbonated hemicarbonate (cHc), which is characterized by a higher CO_3^{2-} and lower OH^- content in the interlayer compared to hemicarbonate (Runčevski et al. 2012). The AFm end member with the interlayer fully occupied by OH^- anions is the hydroxy-AFm (OH-AFm) with the formula $4CaO \cdot Al_2O_3 \cdot xH_2O$. Depending on the relative humidity and exposure temperature, several hydrates of OH-AFm can exist with *x* equal to 7, 11, 13 or 19 and interlayer distances of

5.60 Å (OH-AFm7), 7.35 Å (OH-AFm11), 7.94 Å (OH-AFm13) and 10.70 Å (OH-AFm19), respectively (Aruja 1961, Fischer and Kuzel 1982, Baquerizo et al. 2015). The OH-AFm19 structure is described in the trigonal R-3c space group (for the α_1 polymorph (Aruja 1961)), which space group is also assumed for all other hydrates. OH-AFm is metastable and decomposes to a mixture of katoite ($Ca_3Al_2(OH)_{12}$) and portlandite ($Ca(OH)_2$) at temperatures above 20°C (Lothenbach et al. 2012).

Although the interaction between I^- and CO_3^{2-} in the AFm interlayers has been studied before (Aimoz et al. 2012a), no solubility data were determined and ternary I^-, OH^-, CO_3^{2-} mixtures in AFm interlayers were not considered. To fill this gap, co-precipitation experiments with different concentrations of I^- and its competitor anions CO_3^{2-} and/or OH^- were performed. Characterization of the solids and their solubility properties were used for the construction of solid solution models between I-AFm and the AFm phases mono-, hemicarbonate and hydroxy-AFm more commonly found in hydrated cements.

2. Materials and Methods

2.1 AFm synthesis and characterization

All sample manipulations were performed in a N_2-filled glove box to minimize atmospheric CO_2 contamination. Solutions were prepared using high-purity deionized water (resistivity = 18.2 MΩ cm) generated by a Milli-Q Gradient A10 System (Millipore, Bedford, USA). All chemicals were analytical grade reagents. The following chemicals were used: CaO, Al_2O_3, $CaCO_3$, Na_2CO_3, NaI, and CaI_2 (Sigma-Aldrich, St. Louis, Missouri, USA). Tricalcium aluminate (C_3A) was prepared by mixing appropriate amounts of $CaCO_3$ with Al_2O_3 powder to achieve a molar ratio of 3:1 and by heating the mixture at 800°C for 1h, at 1000°C for another 4h and finally at 1425°C for 24 h. The clinker material was then ground to <63 µm. To ensure that no CO_2 contamination of CaO occurred, the latter compound was heated at 900°C for 12 h prior to the synthesis.

The solid solution series were synthesized by mixing stoichiometric amounts of the starting powder materials C_3A, CaO, and the appropriate $Na_{(2)}$-X (pH~13) or Ca-X (pH~12) salt in MilliQ water or NaOH solution. The goal was to obtain different total iodide mole fractions ($x_I = I^-/(I^- + X^{n-})$ = 0, 0.1, 0.3, 0.5, 0.7, 0.9, 1) with X^{n-} = OH^- and/or CO_3^{2-} for hemicarbonate, monocarbonate and hydroxy-AFm.

The samples were equilibrated for three months, in closed PE-bottles at 20°C on end-over-end shakers (100 rpm). After equilibration, the solid and liquid phases were separated by vacuum filtration through a 0.45 µm nylon filter. The solid phases were dried in a desiccator over a saturated NaOH solution (~8% relative humidity) at room temperature for five to six weeks under initial vacuum.

After drying, the solids were analysed by X-ray powder diffraction (XRPD), thermogravimetric analysis (TGA) and infrared (FTIR) spectroscopy. XRPD analyses were performed on a PANalytical X'Pert Pro MPD diffractometer using CuKα radiation (λ = 1.54184 Å); the diffraction patterns were recorded between $5 < 2\theta < 70°$ with a step size of 0.017° (2θ) and a counting time of 0.6 s per step. Rietveld refinement was conducted using the collected XRPD data of the solid solution samples between monoiodide and hemicarbonate synthesized at pH~12, in order to quantify the evolution of the crystal structure as a function of increasing I^- substitution of the OH^-/CO_3^{2-} groups. In the hemicarbonate structure with the symmetry R-3c, the interlayer hosts OH^-/CO_3^{2-} at the 6-multiplicity symmetry sites with the primary atomic position 2/3, 1/3, 1/12 (Runčevski et al. 2012). For samples with increasing monoiodide mole fraction x_I, first a homogeneous substitution of the interlayer anion group (CO_3^{2-} or OH^-) by I^- was considered, where I^- is placed right on the 6-multiplicity site (occupied by C^{4+} in hemicarbonate) using the configuration published by Rapin et al. (1999). Refinement using this strategy was then compared with the AFm model published in literature, in which the crystal structure of the I-substituted AFm is an alternating layer stacking of hemicarbonate with I-AFm (Aimoz et al. 2012a). Apart from AFm, katoite was also detected by XRPD and its component refined for each sample. The refinement was conducted using the MAUD package (Lutterotti et al. 1999). The experimental condition of the Cu-source lab-XRD was defined via refining the line-broadening parameters using reference data of a CaF_2 standard. Considering the platy morphology of AFm crystals, the crystallite size was described by a two-parameter-Popa model (Lutterotti et al. 1999). It was noted that the (0 0 3) and (0 0 6) diffraction peaks are overwhelmingly strong for some samples, which is most likely due to preferred orientation. Therefore a standard fibre function was used to describe the orientation in the MAUD refinement (Lutterotti et al. 2004, Geng et al. 2018). The lattice parameters and the proportion of I^- substitution were the key information to be fitted from the refinement.

The water content of the solids was determined by TGA measurements, carried out on a TGA/SDTA 851 instrument (Metter Toledo, Switzerland). The samples (~15 mg) were heated under a N_2 atmosphere over the temperature range between 30 and 980°C at a heating rate of 20°C/min. For the calculation of the structural water, the temperature range between 30°C and

~425°C was considered only as mass losses above ~425°C are associated with the removal of CO_2 and possibly HI or I_2. Attenuated total reflectance infrared spectra were recorded in the 4000 to 600 cm^{-1} range on a Bruker Tensor 27 FTIR spectrometer to investigate the absorption bands caused by the carbonate group and the hydrogen bond network.

Immediately after filtration, the pH was measured using a Knick pH-meter with a SE 100 pH/Pt 1000 electrode (Knick, Germany) at room temperature. The electrode was calibrated with NaOH solutions of known concentrations to minimize the alkali error caused by the presence of high Na concentrations (Traynor et al. 2019). The chemical composition of the liquid phases was analysed with a Dionex ICS-3000 ion chromatography system equipped with a Dionex Ion Pac AS25 column for I; a Dionex Ion Pac CS12A column for Na and Ca; and a Dionex Ion Pac CS5A column for Al. The eluents used were 37 mM NaOH solution for I, 1.3 ml of ≥ 99.5% methanesulfonic acid (MSA) per litre water for Na and Ca, and 74 ml of 32% HCl per litre water for Al, respectively (Nedyalkova et al. 2019). The dissolved Al concentrations were quantified in the undiluted solutions; for I, Na and Ca in the case of the pH~12 samples, the samples were diluted by a factor of 1:100. Total inorganic carbon was analysed using a Sievers 5310 C TOC Analyzer equipped with a Sievers 900 Autosampler (GE Analytical Instruments, USA).

2.2 Data interpretation

The measured ion concentrations and pH values in the equilibrium solution were used to calculate the solubility products of the synthesized AFm phases using the thermodynamic modelling program GEMS (Kulik et al. 2013) and the NAGRA/PSI database (Thoenen et al. 2014), including a full speciation calculation. The activity coefficients of the aqueous species were calculated with the built-in extended Debye-Hückel equation. First, the solubility products (log K) of the four end members – I-AFm, hemi-, monocarbonate and OH-AFm were determined referring to Ca^{2+}, AlO_2^-, H_2O, CO_3^{2-}, OH^- and I^-, respectively and solids with 4 Ca within the main layer. For the calculations, the highest possible hydration state of each phase was considered, i.e. 19 H_2O for OH-AFm (Aruja 1961) and 15 H_2O for I-AFm (as determined by dynamic vapour sorption experiments (DVS) in this study; Fig. A.1) - e.g. K_{s0}(I-AFm) = $\{Ca^{2+}\}^4 \{AlO_2^-\}^2 \{I^-\}^2 \{OH^-\}^4 \{H_2O\}^{13}$ for the I-AFm end member where {} denote activity. In the pH~13 samples belonging to the monoiodide-hemicarbonate and monoiodide-monocarbonate solid solution series, measured carbon concentrations were below the detection limit and solubility products were calculated assuming equilibrium conditions with monocarbonate in the case of the hemicarbonate-containing samples and calcite in the case of the monocarbonate-containing samples.

Solubility data of the solid solution series are visualized in the form of Lippmann diagrams, in which the compositions of the liquid and the solid phase in equilibrium with one another are plotted against the total solubility product ΣΠ (Lippmann 1980). ΣΠ of a binary solid solution is defined as the sum of the partial solubility products of each end member (e.g. ΣΠ((I,OH,CO_3)-AFm)) = $\{Ca^{2+}\}^4$ $\{AlO_2^-\}^2$ $[\{I^-\}^2+\{CO_3^{2-}\}^{0.5}+\{OH^-\}]$ $\{OH^-\}^4$ $\{H_2O\}^{12}$ for a sample belonging to the monoiodide-hemicarbonate solid solution series). On a Lippmann diagram, the composition of the solid is represented by the solidus line; the liquid phase composition by the solutus line. The shape of both curves is dependent on the selected solid solution model and the non-ideality of mixing. In the case of non-ideal mixing, the Redlich-Kister (Redlich and Kister 1948) sub-regular model was applied, in which the total Gibbs energy G of a system is defined as:

$$G = \sum_i x_i \mu^\circ{}_i + RT \sum_i x_i ln\, X_i + RT \sum_i x_i ln\, \gamma_i \qquad [1]$$

with x_i = mole fraction of the end member i; μ_i = chemical potential of i; R = universal gas constant; T = temperature and γ_i = activity coefficient of the end member i. The activity coefficients can be fitted using the following equations:

$$ln\, \gamma_1 = x_2^2\,(a_0 + a_1(4x_1 - 1)) \text{ and } ln\, \gamma_2 = x_1^2\,(a_0 - a_1(4x_2 - 1)) \qquad [2]$$

where a_i are the dimensionless Guggenheim parameters (Glynn 2000). The end member mole fraction in the solid x_i in the case of the monoiodide-hemicarbonate series was obtained by Rietveld refinement of the XRPD data. For the monoiodide-hydroxy-AFm and monoiodide-monocarbonate series, x_i was determined by mass balance calculations based on the difference in the I:Al and I:Ca ratios between the initial concentrations in the samples and the measured concentrations in solution after filtration. In the monoiodide-hydroxy-AFm series, significant katoite ($Ca_3Al_2(OH)_{12}$) impurities were detected in some of the samples and a correction was applied. This was done by estimating the amount of katoite from TGA analyses. The x_i values for monoiodide-hydroxy-AFm and monoiodide-monocarbonate series are associated with a large error of about 10 %, in particularly for the cases when secondary phases were present.

In the studied system, an interlayer anion exchange between I^- and CO_3^{2-}/OH^- takes place, i.e. in some cases a substitution by heterovalent anions (1^- vs. 2^-) needs to be taken into account. The exchange reaction can be described using the Vanselow convention (Vanselow 1932) as a substitution of one mole CO_3^{2-} for one mole of I^-, regardless of their charge. A thermodynamic solid solution model based on the Vanselow convention has been shown to adequately describe the mixing between monoiodide and monosulfate, where a heterovalent substitution of I^- for SO_4^{2-} takes place (Aimoz et al. 2012b). Following the Vanselow convention, the end members

are defined as $Ca_2AlI(OH)_6 \cdot 4.5H_2O$ and $Ca_4Al_2(CO_3)_{0.5}(OH)_{13} \cdot 5.5H_2O$ in the case of the monoiodide-hemicarbonate solid solution series. Lippmann diagrams using both, an ideal solid solution model and a sub-regular model with Guggenheim parameters obtained through best fit of experimental data were constructed and compared (see section 3.2.) to find the model which best describes the studied solid solution series.

3. Results and discussion

3.1. AFm end members

The synthesized monoiodide, monocarbonate, hemicarbonate and hydroxy-AFm phases were characterized by XRPD, TGA and liquid phase analyses to confirm the formation of the desired AFm end members. In addition, the effect of pH (~12 and ~13) on their properties was studied. The tendency of the different AFm to incorporate I^- is described in the subsequent section (3.2.).

3.1.1 Monoiodide

The XRPD powder pattern of an I-AFm sample synthesized at pH~13 was refined using the known crystal structure of monoiodide (Rapin et al. 1999) and by placing the I^- anions right on the 6-multiplicity site (primary atomic position 2/3, 1/3, 1/12) in the interlayer (Fig. 1). The refined interlayer distance is 8.86 Å for a composition $3CaO \cdot Al_2O_3 \cdot CaI_2 \cdot 11H_2O$. The presence of about ~20 % of katoite impurities was also detected. The sample is slightly more hydrated than monoiodide reported in literature (Rapin et al. 1999) (11 H_2O vs. 10 H_2O per formula unit), which seems to be an effect of the pH (Fig. 2). When comparing samples synthesized at pH~12 and pH~13, a slight shift of the main diffraction peak towards higher 2Θ values (from 10.0 2Θ Cu Kα (d = 8.8 Å) to 10.2 2Θ Cu Kα (d = 8.6 Å) in the unrefined data) is observed suggesting that at higher pH some additional OH^- might enter the interlayer. Similar observations have also been reported for monosulfate (Matschei et al. 2007a) and Friedel's salt (Renaudin et al. 2015). This OH^- uptake in I-AFm is further supported by TGA analyses, in which a clear difference in the mass loss curves between the pH~12 and pH~13 samples can be seen. Monoiodide synthesized at pH~13 shows an additional water removal step at ~150°C and ~2 wt.% higher total mass loss.

The solubility product for monoiodide at 20°C was determined to be -27.62 ± 0.1 for pH~12 and -27.88 ± 0.4 for pH~13 samples, respectively (Table 1). The equilibration time had no significant effect on the obtained solubility products, in agreement with the observation in a previous study focussing on sulfur- and selenium-containing AFm phases (Nedyalkova et al.

2019). Based on the OH-incorporation observed by XRPD and TGA for the pH~13 samples, the value of -27.62 at pH~12 was preferred for the monoiodide end member. This value is close to the solubility product of -27.14 ± 0.56 (at 23°C) published by Aimoz et al. (2012b).

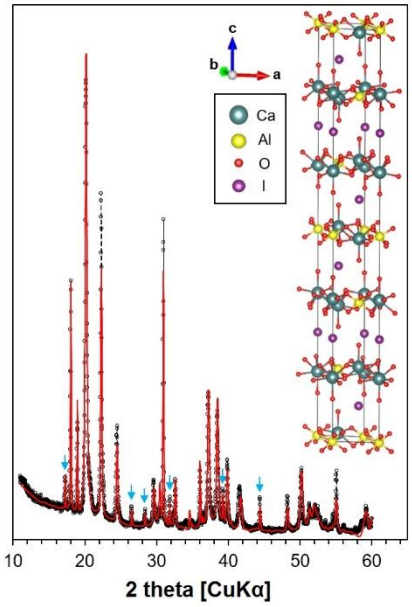

Figure 1: Experimental (black line) and calculated (red line) pattern of the I-AFm sample, synthesized at pH~13, using the published structural model (Rapin et al. 1999) and a direct substitution placing I^- on the 6-multiplicity site. The inset represents the corresponding crystal structure visualized with VESTA (Momma and Izumi 2008). Katoite peaks are marked with blue arrows.

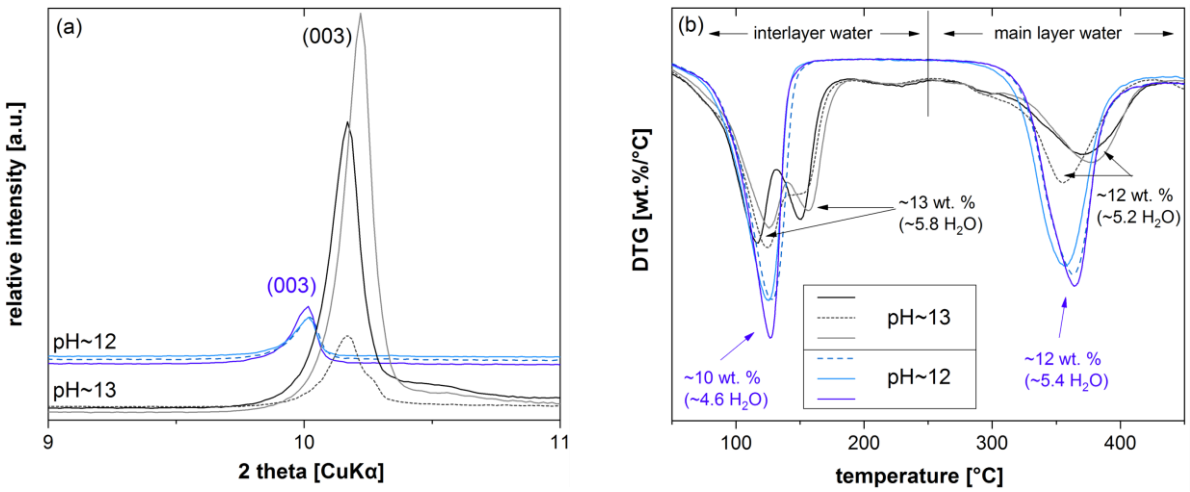

Figure 2: XRPD **(a)** and TGA **(b)** results for monoiodide samples showing the effect of pH (pH~12 vs. pH~13).

3.1.2 Monocarbonate, hemicarbonate and hydroxy-AFm

The monocarbonate samples show the formation of a single AFm phase with an interlayer distance of 7.55 Å (Francois et al. 1998), containing only minor amounts of calcite ($CaCO_3$) as an impurity. The hydration state of the phase was confirmed to be 11 H_2O by TGA. For the pH~12 samples, a mean solubility product of -29.53 ± 1.2 was calculated using the measured carbon concentrations in solution. Measured carbon values for the pH~13 samples were close to the detection limit and the solubility products were calculated with estimated carbon concentrations assuming equilibrium with calcite, resulting in a mean log *K* of -30.43 ± 1.0. The mean solubility product for all monocarbonate samples is thus -30.19 ± 0.8 which is somewhat larger than most of the solubility products of -31.2 to -31.5 reported in literature (Damidot et al. 1994, Lothenbach and Winnefeld 2006, Matschei et al. 2007b), but overlap with these within the error. The difference between the solubility products obtained at pH~12 and pH~13 could indicate that calculated carbon concentrations underestimate the actual carbon concentration and thus the solubility of monocarbonate.

Hemicarbonate samples synthesized at pH~13 consist of hemicarbonate as the main phase coexisting with some carbonated hemicarbonate, visible by a reflection peak at about 11.4° 2Θ (Runčevski et al. 2012). At pH~12 in addition some monocarbonate was detected. The measured mass loss during TGA sums up to 12 H_2O as expected for hemicarbonate. The obtained log *K* of -29.12 ± 0.3 is in good agreement with the values of -29.13 (Matschei et al. 2007b), -29.66 (Damidot et al. 1994) and -29.75 (Lothenbach and Winnefeld 2006) published before.

The low water hydrate OH-AFm13 with *d*-spacing of 7.99 Å is observed in the hydroxy-AFm samples after drying, while in the solution the more hydrated OH-AFm19 is present (Baquerizo et al. 2015). In addition, significant amounts of katoite and portlandite are observed; together they comprise up to about 80 % of the solid in the samples which was confirmed by TGA. Their presence shows that OH-AFm has already substantially decomposed to the thermodynamically more stable katoite and portlandite as reported previously (Matschei et al. 2007b). In fact, the calculated solubility product for the OH-AFm19 is with -26.36 ± 2.0 approximately one log unit lower than previously published values: -25.45 for OH-AFm19 (Lothenbach et al. 2012) as well as -25.40 (Matschei et al. 2007b), -25.35 (Zhang 2000) and -25.00 (Lothenbach et al. 2012) for OH-AFm13 consistent with the observed destabilisation. For the construction of the Lippmann diagrams, the solubility product of -26.4 was used based on the experimental data.

Table 1: Liquid phase analysis and calculated solubility products for the AFm end members monoiodide, hemicarbonate, monocarbonate and hydroxy-AFm. Solubility products for hemicarbonate and monocarbonate at pH~13 were calculated assuming an equilibrium with monocarbonate or calcite, respectively, and are given in *italic*.

Sample	Eq. Time [d]	pH 20°C	Al [mmol/l]	Ca [mmol/l]	I [mmol/l]	C [mmol/l]	Na [mmol/l]	OH [mmol/l]	log K 20°C
monoiodide									
#1	30	13.0	0.362	2.72	103.3	-	218.9	80.80	-27.38
#2	30	13.0	0.406	2.24	102.6	-	213.4	80.80	-27.60
#3	30	13.0	0.396	2.02	100.9	-	213.4	77.79	-27.84
#4	90	13.0	0.036	3.22	74.54	-	206.4	99.63	-29.15
#5	90	12.9	0.323	2.20	102.3	-	218.0	81.53	-28.13
#6	90	13.0	0.152	3.18	94.17	-	219.9	84.97	-27.96
#7	90	13.0	0.284	2.00	87.78	-	219.1	81.44	-28.22
#8	180	12.9	0.182	4.80	89.70	-	211.3	81.79	-27.28
#9	180	12.9	0.274	3.87	84.12	-	201.1	78.67	-27.38
#10	90	11.7	3.85	13.20	12.56	-	0.510	4.42	-27.60
#11	90	11.6	2.76	14.13	24.19	-	0.491	3.46	-27.70
#12	90	11.6	2.70	16.54	25.75	-	0.487	3.14	-27.64
#13	90	11.6	1.26	21.52	40.75	-	0.413	3.33	-27.53
hemicarbonate									
#1	30	13.2	0.342	1.92	-	<.01	212.2	122.7	*-29.04*
#2	30	13.2	0.338	2.24	-	<.01	211.5	127.4	*-28.87*
#3	30	13.2	0.351	2.18	-	<.01	210.1	127.4	*-28.87*
#4	90	13.2	0.080	3.73	-	<.01	203.9	147.0	*-28.97*
#5	90	13.1	0.163	3.91	-	<.01	218.5	129.3	*-28.93*
#6	90	13.2	0.210	2.88	-	<.01	204.1	137.2	*-28.85*
#7	180	13.1	0.299	3.19	-	<.01	209.7	120.7	*-28.83*
#8	180	13.0	0.238	3.67	-	<.01	158.6	99.35	*-28.92*
#9	90	12.6	0.003	18.46	-	0.079	0.425	37.68	-30.28
#10	90	12.7	0.004	19.99	-	0.061	0.496	44.44	-29.68
#11	90	12.7	0.010	20.14	-	0.042	0.499	38.69	-29.10
monocarbonate									
#1	30	13.1	6.05	0.082	-	<.01	203.0	113.7	*-31.93*
#2	30	13.1	5.77	0.226	-	<.01	215.3	113.7	*-30.63*
#3	30	13.1	7.70	0.160	-	<.01	202.8	118.1	*-30.49*
#4	90	13.2	13.03	0.975	-	<.01	208.3	136.0	*-27.84*
#5	90	13.1	3.40	0.529	-	<.01	212.1	124.4	*-30.15*
#6	90	13.1	4.74	0.329	-	<.01	210.2	124.3	*-30.48*
#7	180	13.1	4.00	0.168	-	<.01	207.8	116.1	*-31.51*
#8	180	13.1	2.39	0.532	-	<.01	207.8	116.1	*-30.44*

#9	90	11.9	3.57	3.92	-	0.075	0.439	7.65	-29.35
#10	90	11.8	2.58	3.95	-	0.107	0.501	5.69	-30.06
#11	90	11.9	3.95	5.33	-	0.035	0.521	7.26	-29.17
hydroxy-AFm									
#1	90	13.2	0.343	1.85	-	-	208.5	120.3	-26.20
#2	90	13.2	0.324	1.58	-	-	209.6	125.0	-26.52

*solubility products refer to a solid with 4 Ca in the main layer: K_{s0} = $\{Ca^{2+}\}^4$ $\{AlO_2^-\}^2$ $\{X^-\}^2$ $\{OH^-\}^4$ $\{H_2O\}^x$.

3.2. AFm solid solution series

Solid solution series between monoiodide-hydroxy-AFm, monoiodide-hemicarbonate and monoiodide-monocarbonate were examined at two different pH values of ~12 and ~13. The pH was found to have a minor effect on the observed solubility products as discussed in the previous section. Thus, the focus is on the pH~12 samples as monoiodide synthesized at pH~13 contained additional OH^-, which would complicate the analyses of the solid solution. Moreover, measured carbon concentrations in the equilibrium solution of the pH~13 samples were close to the detection limit and therefore less reliable for the construction of the Lippmann diagrams. The data for the pH~13 samples can be found in the supplementary materials.

3.2.1 Monoiodide-hydroxy-AFm

A series of mixed monoiodide-hydroxy-AFm samples with different monoiodide mole fractions (x_I) were prepared. The XRPD data of the samples show the formation of one main AFm-like phase, in which a decreasing x_I is reflected by a gradual decrease of the interlayer distance from 8.8 Å at x_I = 0.93 (corresponding to the I-AFm end member) down to 8.4 Å at a total iodide fraction of 0.13 (x_I = 0.13) (Fig. 3a). At this composition a second phase with a *d*-value of 7.9 Å appears, corresponding to OH-AFm13 (Fischer and Kuzel 1982). The evolution of the basal reflexion suggests the formation of a solid solution in which an increasing substitution of the larger I^- anion (2.10 Å) by the smaller OH^- anion (1.33 Å (Jenkins and Thakur 1979)) takes place in the AFm interlayer as the amount of iodide decreases. At very low I^- contents two AFm phases coexist – a mixed (I,OH)-AFm and an OH-AFm, indicating the presence of a miscibility gap between $0 \leq x_I \leq 0.2$.

FTIR analyses confirm the presence of one type of AFm phase in the samples with x_I = 0.93 - 0.25. The intensities of the absorption bands show a systematic trend with changing composition (Fig. 3b). In the trigonal structure of the I-AFm end member with a R-3H space group

(Rapin et al. 1999), a prominent absorption band at ~775 cm^{-1} is observed which could be attributed to the Al-O deformation vibration. As composition changes towards smaller x_I values, the band is gradually weakened. The hydrogen bond network, seen in the frequency range between ~3000 and ~3700 cm^{-1}, also changes as a function of x_I. The monoiodide end member is characterized by a strong absorption band at ~3450 cm^{-1} with a shoulder at ~3506 cm^{-1} caused by the stretching vibration of the interlayer water ($v(H_2O)$) as well as an absorption band at ~3624 cm^{-1} with a shoulder at ~3600 cm^{-1} associated with OH stretching of the main layer water (v(OH)). With the decrease of x_I the absorption bands become weaker and less resolved until at x_I = 0.13 an interruption of the trend is observed: $v(H_2O)$ is visible only as a very weak unresolved band between ~3380 and ~3550 cm^{-1} and v(OH) appears as a sharp peak shifted to the left at ~3643 cm^{-1}. This could indicate the limit of the solid solution and the formation of the OH-AFm end member, since the spectra of the sample with x_I = 0.13 closely resembles the spectra of the sample with x_I = 0. In few of the samples, an absorption band at ~1390 cm^{-1} is also observed suggesting some CO_2 contamination.

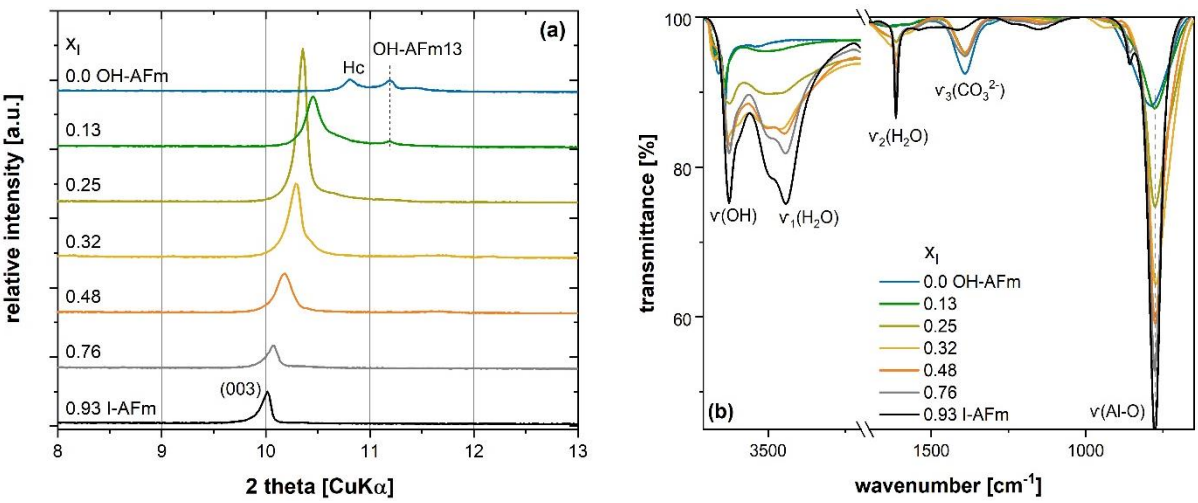

Figure 3: (a) XRD powder pattern of the samples belonging to the monoiodide-hydroxy-AFm solid solution series showing the low 2Θ region and the shift in the basal reflexion. **(b)** FTIR spectra for the same samples.

For the monoiodide-OH-AFm solid solution series a Lippmann diagram was constructed (not shown due to the large uncertainties at low x_I) applying a 1:1 exchange model (with end members $Ca_2AlI(OH)_6 \cdot 4.5H_2O$ and $Ca_2Al(OH)_{6.5} \cdot 6.25H_2O$) since both, iodide and hydroxyl are singly charged anions. In agreement with the miscibility gap observed by XRPD, an ideal solid

solution model could not reproduce the experimental data points. Therefore the model was fitted by the Guggenheim parameters a_0 = -9.1 and a_1 = 6.4, obtained on the basis of the experimentally observed miscibility gap at low I^- concentrations and a best fit of the solidus data. The boundaries of the miscibility gap were thus determined to be $0.05 \leq x_I \leq 0.21$.

3.2.2 Monoiodide-hemicarbonate

XRPD data of the samples with x_I = 0.93 – 0.39 show the formation of a single AFm phase with only minor impurities of katoite and carbonated hemicarbonate. For the samples with x_I = 0.16 and x_I = 0 additional monocarbonate is also observed. The two samples with x_I = 0.93 and x_I = 0.90 contain an AFm phase with an interlayer distance of 8.8 Å corresponding to the monoiodide end member (Rapin et al. 1999). With the decrease of the monoiodide mole fraction (x_I < 0.9) the basal reflexion of the AFm starts to gradually shift from the monoiodide end member towards the hemicarbonate end member (Fig. 4a). The interlayer distance decreases systematically from 8.8 Å at x_I = 0.93 to 8.2 Å at x_I = 0 indicating the presence of a continuous solid solution between the two end members.

FTIR analyses confirm the solid solution formation in the samples. The samples with x_I = 0.93 and x_I = 0.9 show identical spectra consistent with the spectra expected for monoiodide. The intensities of the absorption bands show systematic trend with changing composition between x_I = 0.9 – 0 (Fig. 4b). As the AFm composition changes towards smaller x_I values, the Al-O absorption band at ~775 cm^{-1} in monoiodide is gradually weakened and shifts continuously towards ~740 cm^{-1}, corresponding to the region in which it is found in the hemicarbonate end member. This shift could be attributed to the different environment Al encounters in the samples with decreasing x_I. Although both end members have a trigonal structure, their crystal symmetry differs and is described in the R-3H space group for I-AFm (Rapin et al. 1999) and R-3cH for hemicarbonate (Runčevski et al. 2012). The amount of CO_3^{2-} addition is reflected by the absorption band at ~1390 cm^{-1} caused by the asymmetric stretching mode of the CO_3^{2-} group (v_3-CO_3^{2-}) in the hemicarbonate-containing samples (x_I = 0.9 – 0).

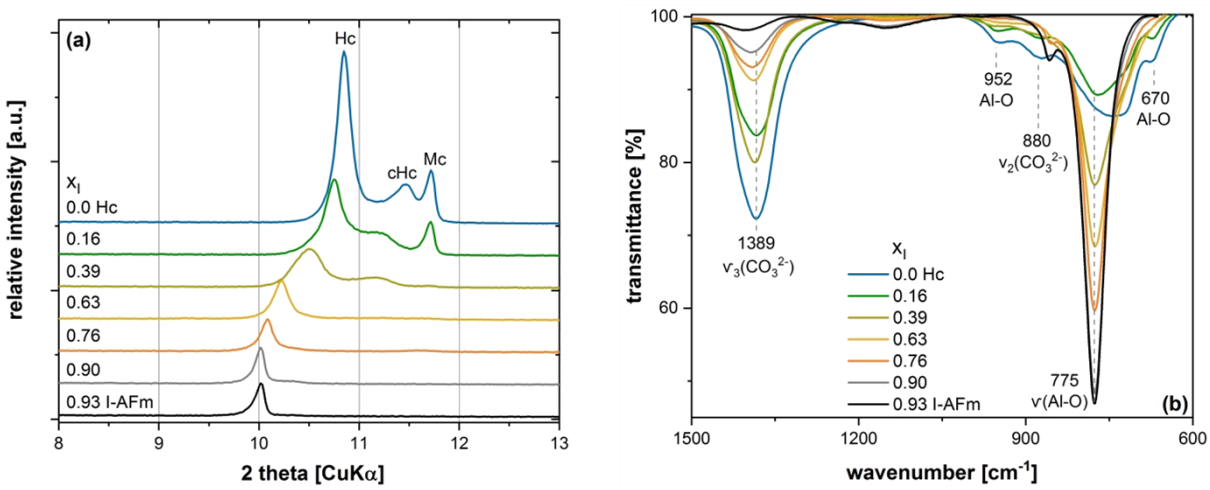

Figure 4: (a) XRD powder pattern of the samples belonging to the monoiodide-hemicarbonate solid solution series showing the evolution of the basal reflexion with changing composition; **(b)** FTIR analyses for the same samples showing the changes in the $v_3(CO_3^{2-})$ and v(Al-O) absorption bands as a function of the monoiodide mole fraction x_I.

As monoiodide and hemicarbonate show different space groups, iodide could be present either in separate interlayers (interstratification) leading to alternating stacking of the layers, as suggested previously in literature (Aimoz et al. 2012a), or alternatively iodide could replace hydroxide/carbonate in hemicarbonate within the same layer. In order to resolve the structure of the observed mixed monoiodide-hemicarbonate AFm phase, Rietveld refinement was conducted on the experimental XRPD data, considering an interstratification of the two end members that gives rise to an AFm with an alternating interlayer stacking of hemicarbonate with I-AFm as proposed by Aimoz et al. (2012a). Assuming such an alternating-layered AFm configuration and a relative I^- dosage of 50% and regular stacking, a structural model was built and its diffraction pattern calculated (Fig. 5a). When refining the experimental data of the sample with nominal I^- dosage of $x_I = 0.5$ (refined $x_I = 0.63$) with the constructed configuration, however, a clear mismatch of the calculated with the measured pattern was noted; strong (003) and (009) peaks were predicted but not observed experimentally (Fig. 5b). Similarly, also (004), (005), (007) and (008) diffraction bands were predicted by the calculation, but not observed in the experimental data. In the R-3cH symmetry of the hemicarbonate structure (Runčevski et al. 2012) the latter peaks are absent. In the alternating-layer model, since the I^--enriched interlayer is thicker than the OH^-/CO_3^{2-}-enriched interlayer, such symmetry no longer exists and the above-mentioned diffractions are allowed. In the experimental XRPD of all monoiodide-hemicarbonate solid solution samples, these peaks remain absent despite the I-dosage, indicating

that the original symmetry of hemicarbonate is conserved during I-uptake. Based on these observations, the alternating-layered model fails to decribe the I-substituted AFm synthesized in this study. It should be noted, however, that stacking disorders could be another reason for the observed discrepancies in the diffraction patterns and that further investigations are needed to confirm the structure of the mixed monoiodide-hemicarbonate AFm samples.

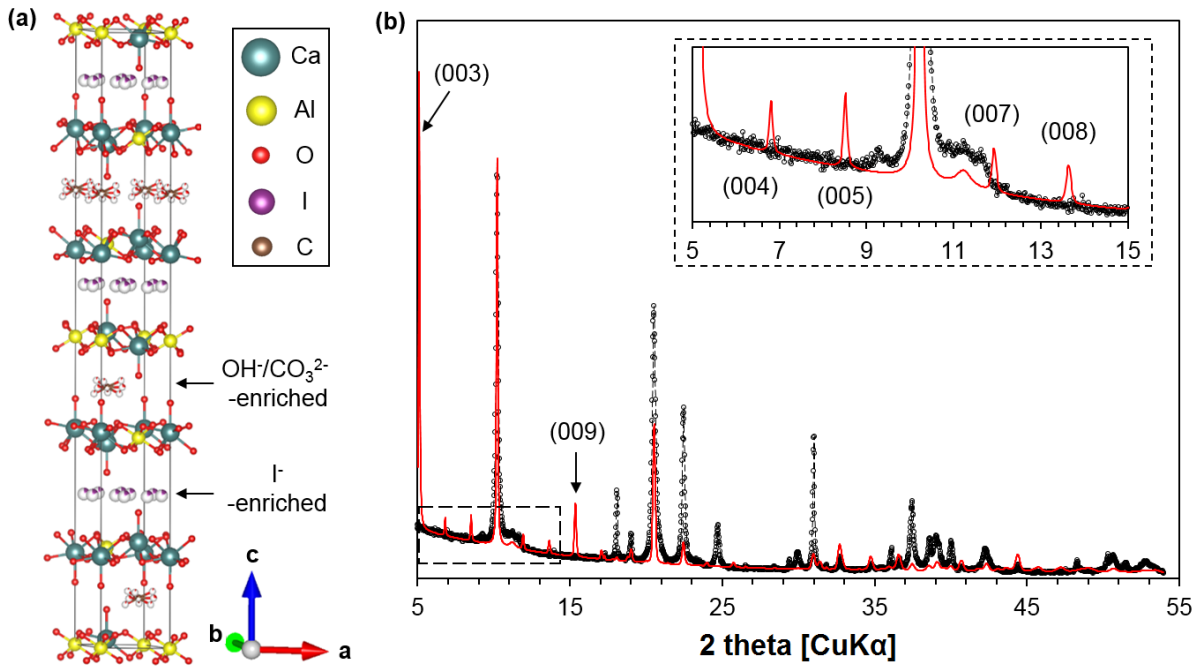

Figure 5: (a) Crystal structure of an alternating-layered AFm phase with x_I = 0.5 and regular stacking of the I^--enriched and OH^-/CO_3^{2-}-enriched interlayer regions. **(b)** Experimental (black line) and calculated (red line) XRPD patterns for a sample with monoiodide mole fraction x_I = 0.63. The dashed square inset shows a magnification of the 2Θ range between 5° and 15°.

To explore the possibility of an interlayer containing simultaneously I^- and OH^-/CO_3^{2-}, the occupancy of I^- (i.e. the probability that the interlayer anion site is occupied by I^-) was fitted based on the XRPD data. The fitted I^- occupancy (refined monoiodide mole fraction) as a function of the nominal monoiodide mole fraction is plotted in Figure 6a, where a continuous increasing of I^- uptake is evidenced. The fitted lattice parameter *a* and *c* are plotted in Figure 6b and 6c, respectively. The lattice parameter *a* shows some fluctuations, but it generally increases with increasing x_I. The overall variance is only ~0.2 Å, which is smaller than 0.4 % of the lattice parameter *a*. On the contrary, the lattice parameter *c* clearly follows an increasing trend with an increase in x_I, i.e. from ~49 Å at x_I = 0 to ~53 Å at x_I = 0.9 and x_I = 0.93. All these observations

indicate that the I^- uptake into the AFm structure is a continuous process between $x_I = 0$ and $x_I = 0.9$. The uptake seems to happen by homogeneous substitution of OH^-/CO_3^{2-} by I^- resulting in an interlayer simultaneously containing I^- and OH^-/CO_3^{2-} anions.

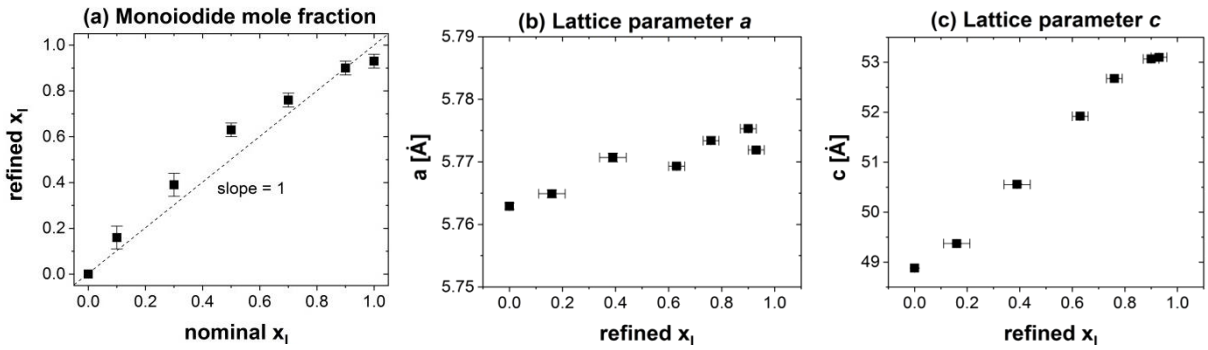

Figure 6: Refinement results showing the amount of I^- incorporated in the structure **(a)** and the lattice parameters *a* **(b)** and *c* **(c)**. The dashed line in **(a)** represents the slope of 1.

The results of the chemical analyses of the equilibrium solution as well as the observations made by XRPD, TGA and FTIR were used for the construction of a Lippmann diagram. XRPD data suggest the formation of a continuous solid solution between the two end members, which is also confirmed by the modelling of the solubility data. The end members were defined according to the Vanselow convention (Vanselow 1932), also applied by Aimoz et al. (2012b) to describe the solid solution formation between monoiodide and monosulfate. An ideal solid solution model did not fully reproduce the experimental solidus data, which lay slightly below the modelled solidus curve (Fig. 7). A regular solid solution model with an interaction parameter a_0 was introduced to fit the solidus data. An acceptable fit was obtained with $a_0 = -1.2$. Experimental solutus data are in a good agreement with the modelled solutus curve.

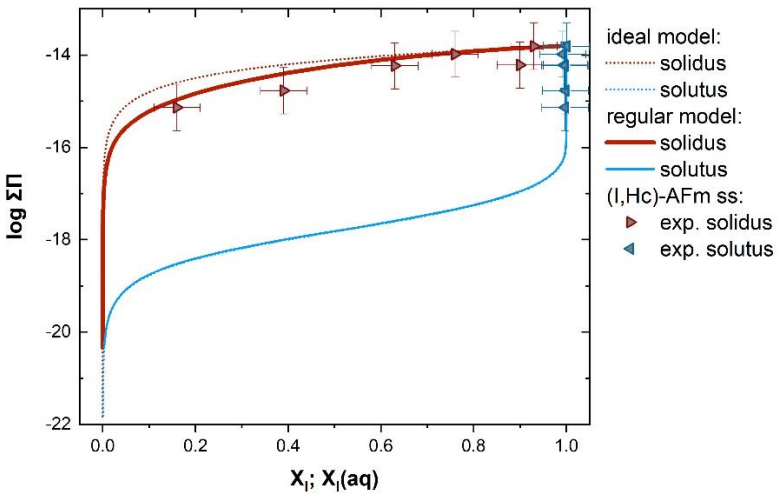

Figure 7: Lippmann diagram for the monoiodide-hemicarbonate solid solution series at 20°C using an ideal-solid solution model (dotted lines) and a solid solution model with the Guggenheim parameter a_0 = -1.2 (solid lines).

3.2.3 Monoiodide-monocarbonate

XRPD data indicate an incomplete miscibility between the two phases in the case of the monoiodide-monocarbonate solid solution series. Samples, synthesized at pH~12, with composition $0.65 \leq x_I \leq 1.0$ consist of one main AFm phase with minor katoite and portlandite impurities. In samples with $x_I \leq 0.44$ additional monocarbonate (accompanied with minor calcite impurities) appears, indicating the presence of a miscibility gap (Fig. 8a). In the composition range $0.09 \leq x_I \leq 0.94$, the basal peak between 10 to 11° 2Θ shifts from the monoiodide end member towards lower d values (and thus higher 2Θ values), consistent with a progressive exchange of the relatively large I^- anion. It is interesting to note that the position of this basal peak corresponds to the basal spacing observed for the monoiodide-hemicarbonate series.

The observations made in XRPD were confirmed by FTIR analyses. The formation of a trigonal AFm phase in the samples with composition $0.09 \leq x_I \leq 0.9$ is indicated by the position of the Al-O absorption band (Fig. 8b). At composition $x_I = 0.44$ additional absorption bands at ~952 cm^{-1}, ~880 cm^{-1}, ~817 cm^{-1}, ~720 cm^{-1} and ~670 cm^{-1} appear indicating the presence of a triclinic monocarbonate as a second phase (Dilnesa et al. 2011). Due to the triclinic structure of monocarbonate, also the $v_3(CO_3^{2-})$ band is split into two components with absorption at ~1362 cm^{-1} and ~1415 cm^{-1} (Fischer and Kuzel 1982), making the phase easily distinguishable from hemicarbonate in FTIR. The band splitting is observed here only for the $x_I = 0$ sample. However, the broad absorption $v_3(CO_3^{2-})$ peaks for the $x_I = 0.09$ and $x_I = 0.44$ samples, would suggest two overlapping signals at ~1362 cm^{-1} and ~1415 cm^{-1} rather than one absorption band at ~1389 cm^{-}

[1]. The splitting of the $\nu_3(CO_3^{2-})$ absorption band with the appearance of monocarbonate in the samples is also visible in the monoiodide-monocarbonate series synthesized at pH~13 (Fig. A2d).

The miscibility gap could be related to the difference in the structure of the two end members (trigonal (I-AFm) vs. triclinic (monocarbonate)), and to the planar arrangement of carbonate in the CO_3-AFm interlayer which prevents the uptake of the larger I^- anion into the structure. A comparable behaviour has been observed for chloride uptake in monocarbonate, where an incomplete solid solution exists between the Cl-AFm end member (Friedel's salt (Terzis et al. 1987)) and monocarbonate with a miscibility gap at low Cl concentrations (e.g. Balonis et al. 2010, Mesbah et al. 2011b).

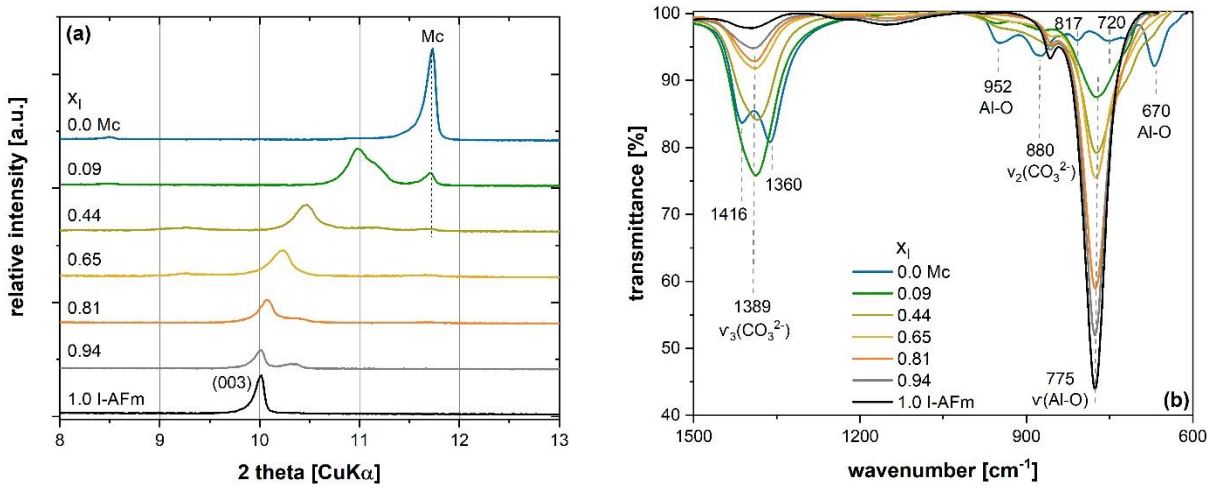

Figure 8: (a) XRD powder pattern of the samples belonging to the monoiodide-monocarbonate solid solution series showing a miscibility gap at $x_I \leq 0.44$. **(b)** FTIR spectra of the same samples confirming the coexistence of a mixed trigonal AFm phase and monocarbonate.

A Lippmann diagram for the monoiodide-monocarbonate solid solution series was constructed applying the solid solution model for monoiodide-hemicarbonate (Fig. 9) (see section 3.3 for discussion). The experimental data has been plotted alongside with the data from the monoiodide-hemicarbonate solid solution series for comparison. The model shows a good fit for the experimental solutus data. Experimental solidus data is well reproduced by the curve of the regular model with the Guggenheim parameter a_0 = -1.2 (solid line in Fig. 9) and shows similar values to the ones obtained for the monoiodide-hemicarbonate series. At x_I < 0.5, a displacement of the solidus data points towards slightly higher total solubility products compared to the

results from the monoiodide-hemicarbonate experimental series can be observed. This could be explained by the fact that with increasing carbonate concentration monocarbonate is being stabilized relative to the (moniodide-hemicarbonate)-AFm phase as also seen by XRPD.

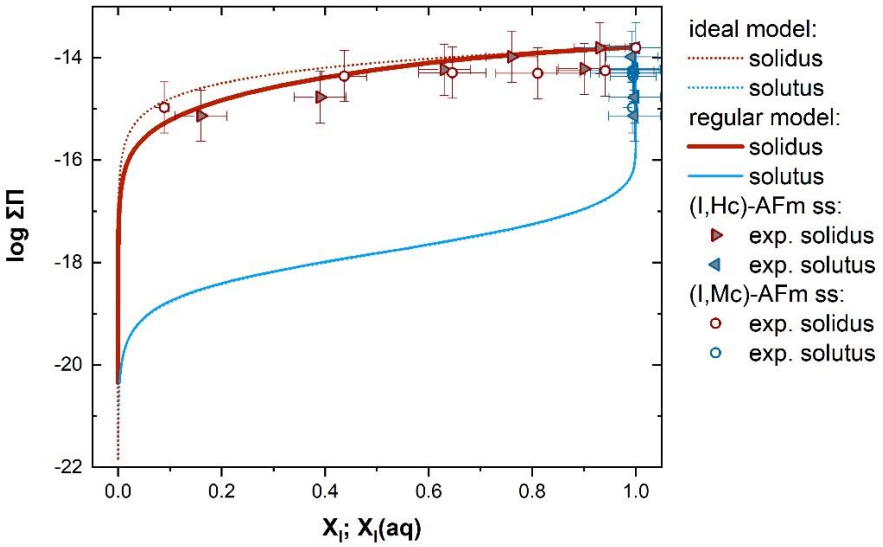

Figure 9: Lippmann diagram for the monoiodide-monocarbonate (circles) solid solution series plotted together with experimental data from the monoiodide-hemicarbonate (triangles) series for comparison. The Lippmann diagram was calculated at 20°C using the ideal (dotted lines) and regular (solid lines) solution model with the Guggenheim parameter a_0 = -1.2 for monoiodide-hemicarbonate.

3.3. Discussion

The addition of I^- to the CaO-Al_2O_3-(CO_2)-H_2O system leads to the formation of solid solutions (complete or incomplete with a miscibility gap) between the different end members. Monoiodide readily incorporates OH^- at high pH and a mixed (I,OH)-AFm seems to be the stable phase at pH~13 and high I^- concentration. At compositions close to the OH-AFm end member, a miscibility gap between monoiodide and OH-AFm exists, which could be explained with the difference in the ionic size between I^- (2.10 Å) and OH^- (1.33 Å (Jenkins and Thakur 1979)). The much larger I^- anion cannot easily substitute for the small OH^- in the OH-AFm lattice.

Small amounts of carbonate are also well incorporated in the AFm structure together with I^- and OH^-, resulting in the precipitation of a mixed monoiodide-hemicarbonate AFm. Higher carbonate concentration, on the other hand, stabilize monocarbonate as previously reported by

Aimoz et al. (2012a). In a comparison between the monoiodide-hemicarbonate and monoiodide-monocarbonate solid solution series (Fig. 10), similar *d*-values are observed, thus suggesting that in both cases the same mixed AFm phase is formed. In the presence of small amounts of carbonate, solid solution formation is promoted and a mixed (I,OH,CO_3)-AFm precipitates in each of the two series, favoured by the same trigonal crystal structure of monoiodide and hemicarbonate. With increasing carbonate concentration, monocarbonate is preferred as hemicarbonate is metastable relative to monocarbonate (Kuzel and Pöllmann 1991, Lothenbach et al. 2008) and both phases do not mix (Pöllmann 2006).

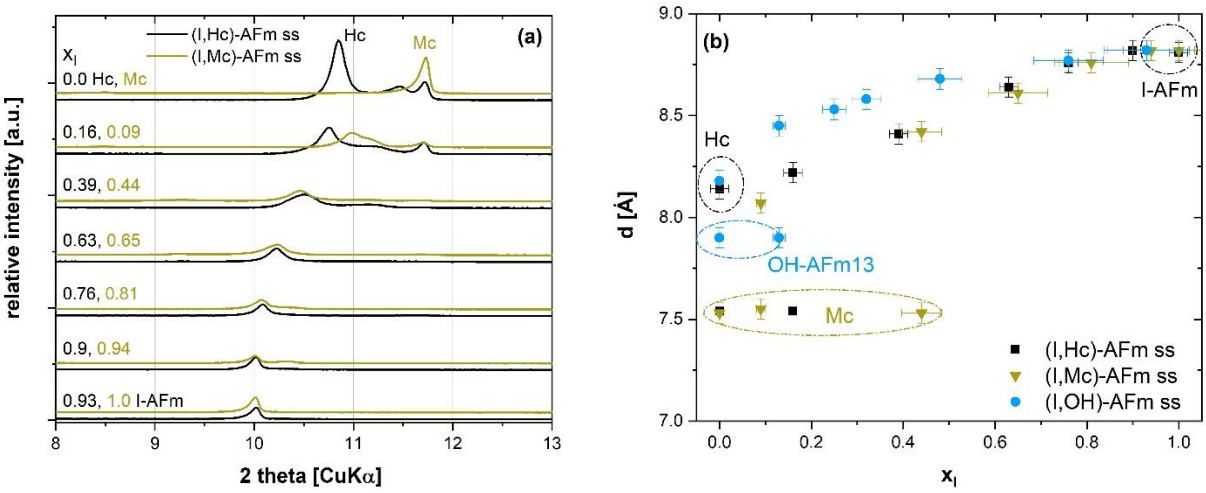

Figure 10: (a) Comparison between the X-ray diffraction patterns of the monoiodide-hemicarbonate (in black) and monoiodide-monocarbonate (in green) solid solution series synthesized at pH~12. **(b)** Evolution of the interlayer distance with changing mole fraction of the I-AFm end member x_I for the three studied solid solution series at pH~12. Hc: hemicarbonate; OH-AFm13: hydroxy-AFm with 13 H_2O; I-AFm: monoiodide; Mc: monocarbonate; ss: solid solution.

4. Conclusions

Experimental data indicate the formation of extensive solid solutions between monoiodide and hydroxy-AFm and monoiodide and hemicarbonate. Whereas the solid solution between monoiodide and hemicarbonate is complete, the presence of a small miscibility gap with composition $0.05 \leq x_I \leq 0.21$ was detected between monoiodide and hydroxy-AFm. Monocarbonate, on the other hand, does not mix with monoiodide and is the stable phase at high carbonate

concentrations, coexisting with a mixed (monoiodide-hemicarbonate)-AFm phase. The solubility of the synthesized phases and their compositions have been visualized in terms of Lippmann diagrams.

In the presence of OH^- and/or small amounts of CO_3^{2-}, iodide is readily incorporated in the AFm interlayers leading to the formation of solid solutions with hydroxy-AFm and hemicarbonate. Both phases, however, are metastable and transform to katoite and portlandite (hydroxy-AFm) or monocarbonate (hemicarbonate) with time. The latter AFm phase, however, is not capable of incorporating iodide. In regard to the safe disposal of iodine-129 in cement-based L/ILW repositories, the results of this study indicate that solid solution formation is an active mechanism over a wide concentration range and the formation of mixed, iodine-bearing AFm phases need to be considered in the modelling approach. The experimental data further implies that the presence of carbonate causes the formation of monocarbonate in the long term, reducing thus the capability of AFm phases to immobilize iodide.

Acknowledgements

The research leading to these results has received funding from the European Union's Horizon 2020 Research and Training Programme of the European Atomic Energy Community (EURATOM) (H2020-NFRP-2014/2015) under grant agreement n° 662147 (CEBAMA). Prof. Guillaume Renaudin (Université Clermont Auvergne, France) is greatly acknowledged for the help with the XRPD analysis of monoiodide. The authors would also like to thank Luigi Brunetti (Empa) and Dr. Frank Winnefeld (Empa) for their assistance with the sample characterization measurements.

5. References

Aimoz, L., E. Wieland, C. Taviot-Guého, R. Dähn, M. Vespa and S. V. Churakov (2012a). "Structural insight into iodide uptake by AFm phases." Environmental Science & Technology **46**(7): 3874-3881, https://doi.org/10.1021/es204470e.

Aimoz, L., D. A. Kulik, E. Wieland, E. Curti, B. Lothenbach and U. Mäder (2012b). "Thermodynamics of AFm-(I_2, SO_4) solid solution and of its end-members in aqueous media." Applied Geochemistry **27**(10): 2117-2129, https://doi.org/10.1016/j.apgeochem.2012.06.006.

Aruja, E. (1961). "The unit cell and space group of 4CaO. Al_2O_3. $19H_2O$ polymorphs." Acta Crystallographica **14**(12): 1213-1216, https://doi.org/10.1107/S0365110X61003557.

Atkins, M. and F. Glasser (1992). "Application of Portland cement-based materials to radioactive waste immobilization." Waste Management **12**(2-3): 105-131, https://doi.org/10.1016/0956-053X(92)90044-J.

Balonis, M., B. Lothenbach, G. Le Saout and F. P. Glasser (2010). "Impact of chloride on the mineralogy of hydrated Portland cement systems." Cement and Concrete Research **40**(7): 1009-1022, https://doi.org/10.1016/j.cemconres.2010.03.002.

Baquerizo, L. G., T. Matschei, K. L. Scrivener, M. Saeidpour and L. Wadsö (2015). "Hydration states of AFm cement phases." Cement and Concrete Research **73**: 143-157, https://doi.org/10.1016/j.cemconres.2015.02.011.

Brown, D. R. and M. W. Grutzeck (1985). "The synthesis and characterization of calcium aluminate monoiodide." Cement and Concrete Research **15**(6): 1068-1078, https://doi.org/10.1016/0008-8846(85)90099-7.

Damidot, D., S. Stronach, A. Kindness, M. Atkins and F. Glasser (1994). "Thermodynamic investigation of the CaO. Al_2O_3. $CaCO_3$. H_2O closed system at 25° C and the influence of Na_2O." Cement and Concrete Research **24**(3): 563-572, https://doi.org/10.1016/0008-8846(94)90145-7.

Dilnesa, B., B. Lothenbach, G. Le Saout, G. Renaudin, A. Mesbah, Y. Filinchuk, A. Wichser and E. Wieland (2011). "Iron in carbonate containing AFm phases." Cement and Concrete Research **41**(3): 311-323, https://doi.org/10.1016/j.cemconres.2010.11.017.

Evans, D. G. and R. C. Slade (2006). Structural aspects of layered double hydroxides. Layered double hydroxides, Springer**:** 1-87, https://doi.org/10.1007/430_005.

Fischer, R. and H.-J. Kuzel (1982). "Reinvestigation of the system C_4A. nH_2O - C_4A. CO_2. nH_2O." Cement and Concrete Research **12**(4): 517-526, https://doi.org/10.1016/0008-8846(82)90066-7.

Francois, M., G. Renaudin and O. Evrard (1998). "A cementitious compound with composition $3CaO.Al_2O_3.CaCO_3.11H_2O$." Acta Crystallographica Section C **54**(9): 1214-1217, https://doi.org/10.1107/S0108270198004223.

Geng, G., R. N. Vasin, J. Li, M. J. A. Qomi, J. Yan, H.-R. Wenk and P. J. Monteiro (2018). "Preferred orientation of calcium aluminosilicate hydrate induced by confined compression." Cement and Concrete Research **113**: 186-196, https://doi.org/10.1016/j.cemconres.2018.09.002.

Glasser, F., A. Kindness and S. Stronach (1999). "Stability and solubility relationships in AFm phases: Part I. Chloride, sulfate and hydroxide." Cement and Concrete Research **29**(6): 861-866, https://doi.org/10.1016/S0008-8846(99)00055-1.

Glynn, P. (2000). "Solid-solution solubilities and thermodynamics: sulfates, carbonates and halides." Reviews in Mineralogy and Geochemistry **40**(1): 481-511, https://doi.org/10.2138/rmg.2000.40.10.

Jenkins, H. and K. Thakur (1979). "Reappraisal of thermochemical radii for complex ions." Journal of Chemical Education **56**(9): 576, https://doi.org/10.1021/ed056p576.

Kulik, D. A., T. Wagner, S. V. Dmytrieva, G. Kosakowski, F. F. Hingerl, K. V. Chudnenko and U. R. Berner (2013). "GEM-Selektor geochemical modeling package: revised algorithm and GEMS3K numerical kernel for coupled simulation codes." Computational Geosciences **17**(1): 1-24, https://doi.org/10.1007/s10596-012-9310-6.

Kuzel, H.-J. (1971). "Zur Frage der Mischkristallbildung von Calciumaluminiumhydroxysalzen." Neues Jahrb. Mineral.: 477-491.

Kuzel, H.-J. and H. Pöllmann (1991). "Hydration of C_3A in the presence of $Ca(OH)_2$, $CaSO_4 \cdot 2H_2O$ and $CaCO_3$." Cement and Concrete Research **21**(5): 885-895, https://doi.org/10.1016/0008-8846(91)90183-I.

Lippmann, F. (1980). "Phase diagrams depicting the aqueous solubility of mineral systems." Neues Jahrb. Mineral. **139**(1): 1-25.

Lothenbach, B., G. Le Saout, E. Gallucci and K. Scrivener (2008). "Influence of limestone on the hydration of Portland cements." Cement and Concrete Research **38**(6): 848-860, https://doi.org/10.1016/j.cemconres.2008.01.002.

Lothenbach, B., L. Pelletier-Chaignat and F. Winnefeld (2012). "Stability in the system CaO–Al_2O_3–H_2O." Cement and Concrete Research **42**(12): 1621-1634, https://doi.org/10.1016/j.cemconres.2012.09.002.

Lothenbach, B. and F. Winnefeld (2006). "Thermodynamic modelling of the hydration of Portland cement." Cement and Concrete Research **36**(2): 209-226, https://doi.org/10.1016/j.cemconres.2005.03.001.

Lutterotti, L., D. Chateigner, S. Ferrari and J. Ricote (2004). "Texture, residual stress and structural analysis of thin films using a combined X-ray analysis." Thin Solid Films **450**(1): 34-41, https://doi.org/10.1016/j.tsf.2003.10.150.

Lutterotti, L., S. Matthies and H. Wenk (1999). "MAUD: a friendly Java program for material analysis using diffraction." IUCr: Newsletter of the CPD **21**(14-15).

Matschei, T., B. Lothenbach and F. Glasser (2007a). "The AFm phase in Portland cement." Cement and Concrete Research **37**(2): 118-130, https://doi.org/10.1016/j.cemconres.2006.10.010.

Matschei, T., B. Lothenbach and F. P. Glasser (2007b). "Thermodynamic properties of Portland cement hydrates in the system CaO–Al_2O_3–SiO_2–$CaSO_4$–$CaCO_3$–H_2O." Cement and Concrete Research **37**(10): 1379-1410, https://doi.org/10.1016/j.cemconres.2007.06.002.

Mesbah, A., M. François, C. Cau-dit-Coumes, F. Frizon, Y. Filinchuk, F. Leroux, J. Ravaux and G. Renaudin (2011a). "Crystal structure of Kuzel's salt $3CaO\cdot Al_2O_3\cdot 1/2CaSO_4\cdot 1/2CaCl_2\cdot 11H_2O$ determined by synchrotron powder diffraction." Cement and Concrete Research **41**(5): 504-509, https://doi.org/10.1016/j.cemconres.2011.01.015.

Mesbah, A., C. Cau-dit-Coumes, F. Frizon, F. Leroux, J. Ravaux and G. Renaudin (2011b). "A new investigation of the Cl^-–CO_3^{2-} substitution in AFm phases." Journal of the American Ceramic Society **94**(6): 1901-1910, https://doi.org/10.1111/j.1551-2916.2010.04305.x.

Momma, K. and F. Izumi (2008). "VESTA: a three-dimensional visualization system for electronic and structural analysis." Journal of Applied Crystallography **41**(3): 653-658, https://doi.org/10.1107/S0021889808012016.

NAGRA (2002). Demonstration of disposal feasibility for spent fuel, vitrified high-level waste and long-lived intermediate level waste, Nagra Technical Report NTB 02-05. Nagra, Wettingen, Switzerland.

Nedyalkova, L., B. Lothenbach, G. Renaudin, U. Mäder and J. Tits (2019). "Effect of redox conditions on the structure and solubility of sulfur- and selenium-AFm phases." Cement and Concrete Research **123**: 105803, https://doi.org/10.1016/j.cemconres.2019.105803.

Pöllmann, H. (2006). "Syntheses, properties and solid solution of ternary lamellar calcium aluminate hydroxi salts (AFm-phases) containing SO_4^{2-}, CO_3^{2-} and OH^-." Neues Jahrbuch für Mineralogie-Abhandlungen: Journal of Mineralogy and Geochemistry **182**(2): 173-181, https://doi.org/10.1127/0077-7757/2006/0042.

Rapin, J.-P., A. Walcarius, G. Lefevre and M. Francois (1999). "A double-layered hydroxide, $3CaO.\ Al_2O_3.\ CaI_2.\ 10H_2O$." Acta Crystallographica Section C: Crystal Structure Communications **55**(12): 1957-1959, https://doi.org/10.1107/S0108270199008665.

Redlich, O. and A. Kister (1948). "Algebraic representation of thermodynamic properties and the classification of solutions." Industrial & Engineering Chemistry **40**(2): 345-348, https://doi.org/10.1021/ie50458a036.

Renaudin, G., M. Francois and O. Evrard (1999). "Order and disorder in the lamellar hydrated tetracalcium monocarboaluminate compound." Cement and Concrete Research **29**(1): 63-69, https://doi.org/10.1016/S0008-8846(98)00184-7.

Renaudin, G., A. Mesbah, B. Dilnesa, M. Francois and B. Lothenbach (2015). "Crystal chemistry of iron containing cementitious AFm layered hydrates." Current Inorganic Chemistry **5**(3): 184-193, https://doi.org/10.2174/1877944105666150420235831.

Runčevski, T., R. E. Dinnebier, O. V. Magdysyuk and H. Pöllmann (2012). "Crystal structures of calcium hemicarboaluminate and carbonated calcium hemicarboaluminate from synchrotron powder diffraction data." Acta Crystallographica Section B: Structural Science **68**(5): 493-500, https://doi.org/10.1107/S010876811203042X.

Taylor, H. F. (1997). Cement chemistry, Thomas Telford.

Terzis, A., S. Filippakis, H.-J. Kuzel and H. Burzlaff (1987). "The crystal structure of $Ca_2Al(OH)_6Cl\cdot 2H_2O$." Zeitschrift für Kristallographie-Crystalline Materials **181**(1-4): 29-34, https://doi.org/10.1524/zkri.1987.181.14.29.

Thoenen, T., W. Hummel, U. Berner and E. Curti (2014). "The PSI/Nagra chemical thermodynamic database 12/07." PSI report 14-04: 14-49.

Toyohara, M., M. Kaneko, H. Ueda, N. Mitsutsuka, H. Fujihara, T. Murase and N. Saito (2000). "Iodine sorption onto mixed solid alumina cement and calcium compounds." Journal of Nuclear Science and Technology **37**(11): 970-978, https://doi.org/10.1080/18811248.2000.9714980.

Traynor, B., H. Uvegi, E. Olivetti, B. Lothenbach and R. J. Myers (2019). "Methodology for pH measurement in high alkali cementitious systems." Cement and Concrete Research **submitted**.

Vanselow, A. P. (1932). "Equilibria of the base-exchange reactions of bentonites, permutites, soil colloids, and zeolites." Soil Science **33**(2): 95-114, https://doi.org/10.1097/00010694-193202000-00002.

Wersin, P., L. H. Johnson, B. Schwyn, U. Berner and E. Curti (2003). Redox conditions in the near field of a repository for SF/HLW and ILW in Opalinus clay, Nagra Technical Report NTB 02-13. Nagra, Wettingen, Switzerland.

Zajac, M., A. Rossberg, G. Le Saout and B. Lothenbach (2014). "Influence of limestone and anhydrite on the hydration of Portland cements." Cement and Concrete Composites **46**: 99-108, https://doi.org/10.1016/j.cemconcomp.2013.11.007.

Zhang, M. (2000). "Incorporation of oxyanionic B, Cr, Mo, and Se into hydrocalumite and ettringite, application to cementitious systems." PhD Thesis at the University of Waterloo, Ontario, Canada.

6. Appendix

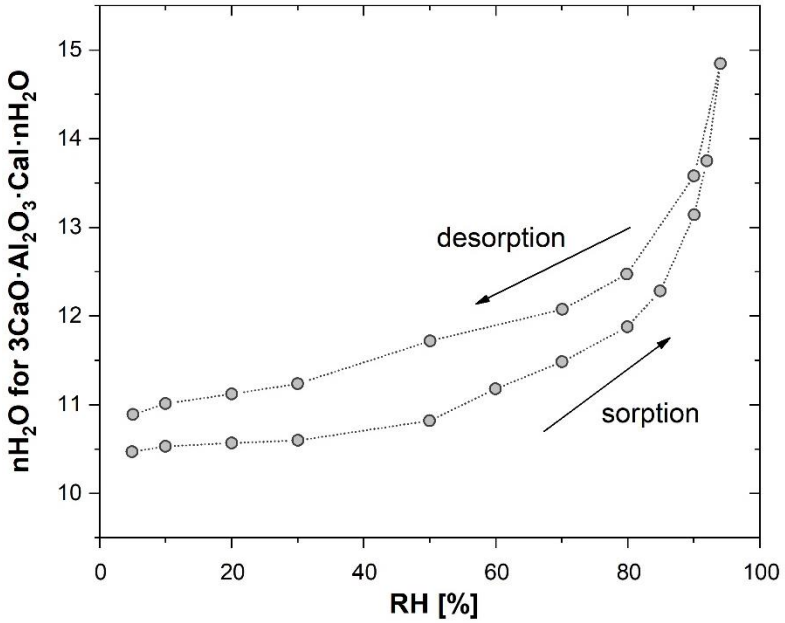

Figure A.1: Sorption isotherm for monoiodide (pH~13) measured at 25°C on a VTI-SA Dynamic Vapour Sorption (DVS) apparatus (TA Inc, USA). The relative humidity (RH) was varied between 5 and 95 %. The graph was normalized to 10 H_2O based on the structure reported for monoiodide (Rapin et al. 1999).

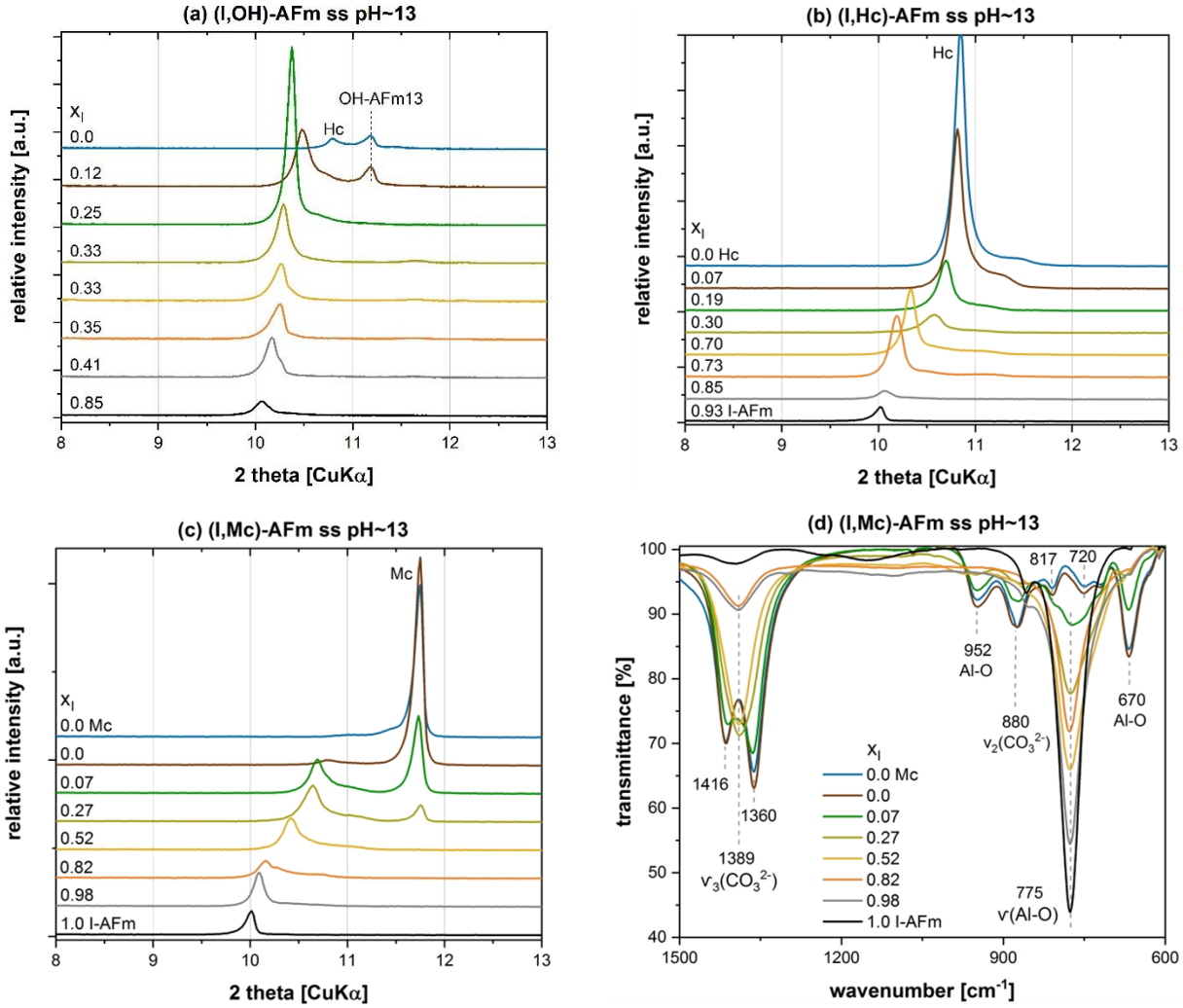

Figure A.2: XRPD pattern of the monoiodide-hydroxy-AFm **(a)**, monoiodide-hemicarbonate **(b)** and monoiodide-monocarbonate-AFm **(c)** solid solution series synthesized at pH~13 and 20°C; **(d)** FTIR spectra of the monoiodide-monocarbonate-AFm series showing the splitting of the $v_3(CO_3^{2-})$ band with the appearance of monocarbonate. Hc: hemicarbonate, I-AFm: monoiodide, Mc: monocarbonate, OH-AFm13: hydroxy-AFm with 13 H_2O.

Table A.1: Dissolution reactions used to calculate the solubility products (log K_{s0}).

Phase	Dissolution reaction		log K_{s0} 20°C
monoiodide	$Ca_4Al_2I_2(OH)_{12}\cdot 9H_2O$	$\rightarrow 4Ca^{2+} + 2AlO_2^- + 2I^- + 4OH^- + 13H_2O$	-27.6 ± 0.1
hydroxy-AFm	$Ca_4Al_2(OH)_{14}\cdot 12H_2O$	$\rightarrow 4Ca^{2+} + 2AlO_2^- + 6OH^- + 16H_2O$	-26.4 ± 2.0
hemicarbonate	$Ca_4Al_2(CO_3)_{0.5}(OH)_{13}\cdot 5.5H_2O$	$\rightarrow 4Ca^{2+} + 2AlO_2^- + 0.5(CO_3)^{2-} + 5OH^- + 9.5H_2O$	-29.1 ± 0.3
monocarbonate	$Ca_4Al_2(CO_3)(OH)_{12}\cdot 5H_2O$	$\rightarrow 4Ca^{2+} + 2AlO_2^- + CO_3^{2-} + 4OH^- + 9H_2O$	-30.2 ± 0.8

Table A.2: Refinement results for the samples belonging to the monoiodide-hemicarbonate-AFm solid solution series synthesized at pH~12.

nominal x_I	refined x_I	*a* [Å]	*c* [Å]	(I,Hc)-AFm [%]	katoite [%]	cHc [%]	Mc [%]
0.0	0.00 ± 0.00	5.76 ± 0.001	48.88 ± 0.003	50 ± 5	9 ± 2	25 ± 5	16 ± 5
0.1	0.16 ± 0.05	5.76 ± 0.001	49.37 ± 0.005	58 ± 5	11 ± 2	18 ± 5	13 ± 5
0.3	0.39 ± 0.05	5.77 ± 0.001	50.56 ± 0.006	53 ± 10	6 ± 2	41 ± 15	0 ± 2
0.5	0.63 ± 0.03	5.77 ± 0.000	51.92 ± 0.003	86 ± 5	2 ± 2	12 ± 5	0 ± 2
0.7	0.76 ± 0.03	5.77 ± 0.001	52.68 ± 0.005	100 ± 2	0 ± 0	0 ± 2	0 ± 0
0.9	0.90 ± 0.03	5.78 ± 0.000	53.07 ± 0.002	100 ± 2	0 ± 0	0 ± 2	0 ± 0
1.0	0.93 ± 0.03	5.77 ± 0.000	53.10 ± 0.003	100 ± 0	0 ± 0	0 ± 0	0 ± 0

Table A.3: Liquid phase analysis of the samples belonging to the monoiodide-hydroxy-AFm solid solution series.

Sample x_I	Eq. Time [d]	pH 20°C	Al [mmol/l]	Ca [mmol/l]	I [mmol/l]	Na [mmol/l]	OH [mmol/l]
0.76	90	12.3	0.036	12.39	32.17	20.14	16.47
0.48	90	12.7	0.009	8.20	33.29	60.26	38.83
0.32	90	12.9	0.014	4.72	19.54	99.19	67.02
0.25	90	13.1	0.152	2.23	10.31	143.9	91.54
0.13	90	13.1	0.262	1.65	5.98	183.8	111.2
0.35	90	13.0	0.120	2.03	83.08	216.7	84.68
0.33	90	13.1	0.068	2.33	52.22	215.5	98.97
0.33	90	13.1	0.195	1.66	21.85	208.3	111.2
0.25	90	13.1	0.309	1.61	11.19	208.4	115.7
0.12	90	13.1	0.325	1.78	6.62	203.0	107.0

Table A.4: Liquid phase analysis of the samples belonging to the monoiodide-hemicarbonate solid solution series.

Sample x_I	Eq. Time [d]	pH 20°C	Al [mmol/l]	Ca [mmol/l]	I [mmol/l]	C [mmol/l]	Na [mmol/l]	OH [mmol/l]
0.90	90	11.7	2.51	12.49	17.19	0.081	0.459	4.45
0.76	90	11.9	2.45	10.11	10.62	0.084	0.496	6.55
0.63	90	12.0	1.40	9.13	6.97	0.022	0.492	9.27
0.39	90	12.3	0.040	16.16	8.98	0.017	0.480	17.87
0.16	90	12.5	0.009	18.24	2.18	0.006	0.503	27.33
0.73	90	13.0	0.181	2.28	87.74	<.01	216.2	88.43

0.70	90	13.1	0.173	1.31	68.23	<.01	216.4	103.8
0.30	90	13.1	0.102	3.32	46.02	<.01	216.4	112.4
0.19	90	13.1	0.096	2.69	25.51	<.01	220.7	121.7
0.07	90	13.2	0.081	1.90	8.835	<.01	209.4	131.9

Table A.5: Liquid phase analysis of the samples belonging to the monoiodide-monocarbonate solid solution series.

Sample x_I	Eq. Time [d]	pH 20°C	Al [mmol/l]	Ca [mmol/l]	I [mmol/l]	C [mmol/l]	Na [mmol/l]	OH [mmol/l]
0.94	90	11.6	3.06	13.64	21.57	0.081	0.461	3.08
0.81	90	11.7	4.01	10.17	11.87	0.077	0.443	4.38
0.65	90	11.9	3.31	9.11	9.11	0.057	0.468	6.22
0.44	90	12.0	2.72	7.87	5.74	0.027	0.456	8.83
0.09	90	12.0	3.65	5.59	3.77	0.025	0.498	7.85
0.82	90	13.0	0.080	3.92	97.63	<.01	213.2	95.06
0.52	90	13.0	0.166	3.99	88.20	<.01	214.0	95.06
0.27	90	13.0	0.186	3.29	72.91	<.01	217.9	98.77
0.07	90	13.0	0.070	2.99	53.12	<.01	212.8	106.6
0.0	90	13.1	0.566	0.681	20.65	<.01	209.5	119.7